Dissolution of Biogenic and Synthetic UO₂ under Varied Reducing Conditions

KAI-UWE ULRICH,*,† ABHAS SINGH,†
ELEANOR J. SCHOFIELD,‡
JOHN R. BARGAR,‡ HARISH VEERAMANI,§
JONATHAN O. SHARP,§
RIZLAN BERNIER-LATMANI,§ AND
DANIEL E. GIAMMAR†

*Department of Energy, Environmental and Chemical
Engineering, Washington University, One Brookings Drive, St.
Louis, Missouri 63130, Stanford Synchrotron Radiation
Laboratory, SLAC, 2575 Sand Hill Road, Menlo Park,
California 94025, and Ecole Polytechnique Fédérale de
Lausanne, CH-1015 Lausanne, Switzerland*

The chemical stability of biogenic UO₂, a nanoparticulate
product of environmental bioremediation, may be impacted by
the particles' surface free energy, structural defects, and
compositional variability in analogy to abiotic UO_{2+x} ($0 \leq x \leq
0.25$). This study quantifies and compares intrinsic solubility
and dissolution rate constants of biogenic nano-UO₂ and synthetic
bulk $UO_{2.00}$, taking molecular-scale structure into account.
Rates were determined under anoxic conditions as a function
of pH and dissolved inorganic carbon in continuous-flow
experiments. The dissolution rates of biogenic and synthetic
UO₂ solids were lowest at near neutral pH and increased with
decreasing pH. Similar surface area-normalized rates of
biogenic and synthetic UO₂ suggest comparable reactive surface
site densities. This finding is consistent with the identified
structural homology of biogenic UO₂ and stoichiometric $UO_{2.00}$.
Compared to carbonate-free anoxic conditions, dissolved
inorganic carbon accelerated the dissolution rate of biogenic
UO₂ by 3 orders of magnitude. This phenomenon suggests
continuous surface oxidation of U(IV) to U(VI), with detachment
of U(VI) as the rate-determining step in dissolution. Although
reducing conditions were maintained throughout the experiments,
the UO₂ surface can be oxidized by water and radiogenic
oxidants. Even in anoxic aquifers, UO₂ dissolution may be controlled
by surface U(VI) rather than U(IV) phases.

Introduction

The remediation of uranium-contaminated soils and ground-
water is an environmental challenge worldwide. Because
uraninite (nominally UO₂) is stable over geological time spans
in low-temperature geological and sedimentary environ-
ments (*1, 2*), the formation of UO₂ in the ground has been
proposed to immobilize U contamination *in situ*. Dissimila-
tory metal- and sulfate-reducing bacteria can couple the

reduction of dissolved U(VI) to the oxidation of organic matter
and H₂, resulting in the precipitation of biogenic UO₂ (bio-
UO₂) (*3–5*). The stimulation of such bacteria has been tested
for subsurface remediation of U-contaminated aquifers and
sediments (*6–8*).

Bioremediation can be successful if dissolution and/or
reoxidation of bio-UO₂ are slow enough to keep dissolved U
concentrations below regulatory threshold values, such as
the U.S. EPA drinking water standard of 30 μg/L (*9*). However,
recent studies on the remobilization of U after microbial
reduction of U(VI) in soils and sediments have reported
oxidation-driven U release on time-scales of six hours to
several weeks (*10, 11*). Oxidation of U(IV) was even observed
in field sediments that included microbes capable of U(VI)
reduction (*12*). Because these studies investigated complex
media, thermodynamic and kinetic properties of bio-UO₂
solids are unknown. Spectroscopic data have recently been
used to estimate lattice contraction and surface stress of bio-
UO₂ nanoparticles, predicting a 10^9-fold increase in solubility
compared to crystalline uraninite (*13*). Such a dramatic
change in stability would render bio-UO₂ a relatively poor
sink phase even under reducing conditions. Thus, funda-
mental knowledge on the key properties predicting the
stability of bio-UO₂ nanoparticles is required.

The objectives of this study are to characterize intrinsic
solubility and dissolution kinetics of bio-UO₂ nanoparticles
under reducing conditions, where UO₂ materials are expected
to be most stable. Dissolution rates of bio-UO₂ and its
synthetic analog are determined in the absence and presence
of inorganic carbon and as a function of pH. To elucidate the
impact of particle size, structure, and stoichiometry on
intrinsic properties and dissolution mechanisms of bio-UO₂,
relevant results of detailed structural studies (*14*) are also
presented.

Experimental Section

Materials. All reagents used in this study were certified
analytical grade or better. The preparation of UO₂ materials
and all aliquot transfer actions took place in an anaerobic
chamber (Coy Laboratory Products Inc.) containing a gas
mixture of 95 vol% N₂(g) and 5 vol% H₂(g) that was circulated
through a Pd catalyst and silica gel. The O₂(g) fugacity was
monitored by a Coy sensor and maintained below the
detection limit of 10^{-6} bar (1 ppm), representing an O₂(aq)
equilibrium concentration of $<10^{-8.9}$ M. The preparation
protocols for synthetic uraninite (syn-UO₂) and bio-UO₂ are
given in the Supporting Information (SI). In brief, syn-UO₂
powder was produced by chemical reduction of studtite
($UO_2O_2 \cdot 4H_2O_{(s)}$) with heated H₂(g). Bio-UO₂ was gained from
enzymatic reduction of uranyl carbonate coupled to lactate
oxidation under anaerobic conditions both at pH 6.3 and 8.0
using *Shewanella oneidensis* strain MR-1. The resulting bio-
UO₂ solid was isolated from the biomass after treatment
involving sonication and lysozyme or 1 M NaOH. The NaOH-
treated material was used in this study unless otherwise noted.
A reference sample of stoichiometric $syn-UO_{2.00}$ was provided
courtesy of David Clark at Los Alamos National Laboratory
(cf. Table 1 for nomenclature of study materials).

Dissolution Experiments. UO₂ dissolution under continu-
ous flow prevents accumulation of dissolved U and maintains
undersaturated conditions in a continuous-flow reactor (CFR).
A detailed description of the setup is given in the SI (Figure S1).
Custom-made CFRs of 12.58 mL volume were magnetically
stirred and operated in the dark at room temperature (20 ± 1
°C). Influent flow rates were set between 0.2 and 2.1 mL/min
and gravimetrically monitored based on effluent volume. These

* Corresponding author phone: 314-935-6234; fax: 314-935-7211;
e-mail: k.ulrich@seas.wustl.edu.
† Washington University in St. Louis.
‡ Stanford Synchrotron Radiation Laboratory.
§ Ecole Polytechnique Fédérale de Lausanne.

TABLE 1. Summary of UO$_2$ Synthesis and Main Characteristics of the Study Materials

UO$_2$ material	biogenic		abiotic	
oxidant	U(VI)$_{(aq)}$, mainly UO$_2$(CO$_3$)$_3^{4-}$		solid studtite (UO$_2$O$_2\cdot$4H$_2$O)	
reductant	*Shewanella oneidensis* MR1		H$_{2(g)}$ at 400 °C	
pH of U(VI) reduction	6.3	8.0		
Sample ID	**bio6-UO$_2$**	**bio8-UO$_2$**	**synA-UO$_2$**[a]	**synB-UO$_2$**
specific surface area (m^2/g)	50.14[b]		5.93[b]	3.1[c]
crystallite size range (nm)	1.5 − 3.5[d]		92 − 200[e]	600 − 800[f]

[a] Courtesy of Dan Schwarz and David Clark, Los Alamos National Laboratory. [b] Multipoint N$_2$−BET. [c] Calculated from particle morphology visualized by scanning electron microscopy (SEM). [d] Derived from high-resolution transmission electron microscopy (HR-TEM) and synchrotron-based powder diffraction (SR-PD). [e] Lower value calculated from SSA, higher value taken from SEM images (upper limit). [f] Based on SEM images.

flow rates were chosen to provide short residence times to keep the H$_2$ level in the CFR high enough to sustain a reducing environment and to achieve steady-state effluent dissolved U concentrations far below saturation (15). The influent [O$_2$]$_{diss}$ was monitored by a dissolved oxygen sensor (Microelectrodes, Inc.), and the U-concentration was periodically measured to establish that the feed solution, tubing, and reactor materials released negligible uranium. The effluent passed through 0.2 μm (polycarbonate) or 0.025 μm (mixed cellulose ester, both Millipore) filter membranes at the CFR exit and was continuously collected for pH measurement and U analyses.

The UO$_2$ dissolution was studied at chemical conditions relevant to groundwater remediation. Reducing conditions were equilibrated in the feed solution by bubbling a mixture of 95 vol% N$_2$ and 5 vol% H$_2$ in presence of a Pd catalyst. The first step in all experiments used an influent at near neutral pH (stabilized with HEPES or TAPS organic buffer) that was applied for up to 40 residence times. In selected experiments, the continuous flow was then stopped and reactors were run in batch mode for 4 d to determine the difference between the steady-state, [U]$_{ss}$, and equilibrium, [U]$_{eq}$, concentrations. In other experiments, further continuous-flow steps provided either 1 mM anoxic NaHCO$_3$ or NaCl and diluted HCl in the feed solution. Because the solid concentration of the bio-UO$_2$ suspensions was initially unknown, the residual UO$_2$ solid was digested in strong acid and analyzed for total U.

Analysis. The total U concentrations of the residual solids, the influent, [U]$_{in}$, and the effluent were determined in a 0.1 M HNO$_3$ matrix by ICP-MS (Agilent 7500*ce*) with a detection limit of <10 ng/L. The dissolved U(VI) concentration was spectrophotometrically determined in selected samples using the Bromo-PADAP method (16) with a detection limit of ∼0.1 μM. The syn-UO$_2$ material was analyzed by XRD (Rigaku D-MAX/A) using Cu kα radiation, and imaged by scanning electron microscopy (Hitachi S-4500) of Au-coated UO$_2$ particles dispersed directly on sample mounts or loaded on pieces of filters. U L$_{III}$-edge X-ray absorption data on syn-UO$_2$ and bio-UO$_2$ were collected at SSRL beamlines 10-2 and 11-2 equipped with a Si(220) double-crystal monochromator which was calibrated by using yttrium foil. Extended X-ray absorption fine structure (EXAFS) spectra were background subtracted, splined, and analyzed using SIXPack (17) with FEFF8 backscattering phase and amplitude functions (18). *In-situ* synchrotron powder diffraction (SR-PD) data were collected in transmission geometry on SSRL beamline 7-2. The incident X-ray beam was set to 16.1 keV (λ = 0.77 Å) and the diffractometer was calibrated with LaB$_6$. Wet samples were loaded into quartz capillaries. Data were collected in Q-space of 0.02 Å^{-1} intervals out to ∼14.5 Å^{-1}. Multiple scans were taken and averaged in order to improve the signal-to-noise ratio.

Dissolution Rate Calculation. The dissolution rate of UO$_2$ solid loaded into a CFR can be calculated from the mass balance equation (eq 1) once steady-state is reached, i.e., $d[U]_{eff}/dt = 0$. This takes at least 5 residence times, $\tau = VQ^{-1}$ (min).

$$V \times \frac{d[U]_{eff}}{dt} = Q \times [U]_{in} - Q \times [U]_{eff} + V \times R_d \quad (1)$$

In eq 1 [U]$_{eff}$ and [U]$_{in}$ (mol L^{-1}) are the U concentrations in the effluent and influent, V (L) is the reactor volume, Q (L min^{-1}) is the flow rate, and R_d (mol L^{-1} min^{-1}) is the rate of U release to solution from UO$_2$ dissolution. Assuming [U]$_{in}$ is zero, the dissolution rate can be calculated as follows:

$$R_m = \frac{Q \times [U]_{ss}}{V \times [solid]} \quad (2)$$

$$R_n = \frac{Q \times [U]_{ss}}{V \times SSA \times [solid]} \quad (3)$$

where R_m (mol g^{-1} min^{-1}) and R_n (mol m^{-2} min^{-1}) are the dissolution rates normalized to mass and specific surface area, SSA (m^2 g^{-1}), respectively, and [solid] (g L^{-1}) is the mass concentration of UO$_2$ in the reactor. The rate calculation accounts for the changes in [solid] and SSA with time that result from UO$_2$ dissolution (see SI for details). The reaction rate constant, k (mol m^{-2} min^{-1}), in a general rate equation that accounts for the reaction affinity (i.e., distance to equilibrium with respect to eq 4) can be derived from eq 5.

$$UO_{2(s)} + 4 H^+ \rightarrow U^{4+} + 2 H_2O \quad (4)$$
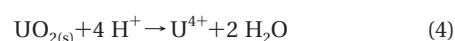
$$R_n = k \times SSA \times [solid]\left(1 - \frac{[U^{4+}]_{eff}[H^+]_{eff}}{K_{sp,UO_2}}\right) = k \times SSA \times [solid] \times$$
$$\left(1 - \frac{[U]_{eff}}{[U]_{eq}}\right) \quad (5)$$

Calculation of [U]$_{eq}$ is based on thermodynamic data given in Table S1 in the SI. A numerical solution to predict [U]$_{eff}$, [solid], and SSA as a function of time was developed and used to determine optimal values of k (see SI for details).

Results and Discussion

Structural Properties. The synthetic UO$_2$ materials were brown or blackish brown powders consisting of a highly crystalline face-centered cubic lattice as identified by powder XRD (Figure S3, SI). The synthetic UO$_2$ particle morphology and size were visualized by SEM (Figure S2, SI). Particles had mean diameters of about 100−200 nm (synA-UO$_2$) or 600−800 nm (synB-UO$_2$). Bio-UO$_2$ particles had diameters of 1.5−3.5 nm as determined by Fourier filtered HR-TEM images (14). Multipoint N$_2$−BET measured a SSA of 50.14 m^2 g^{-1} for bio-UO$_2$ and 5.93 m^2 g^{-1} for synA-UO$_2$. A mean SSA of 3.1 m^2 g^{-1} was calculated for synB-UO$_2$ from the morphology of the particles observed by SEM. This number is likely to represent
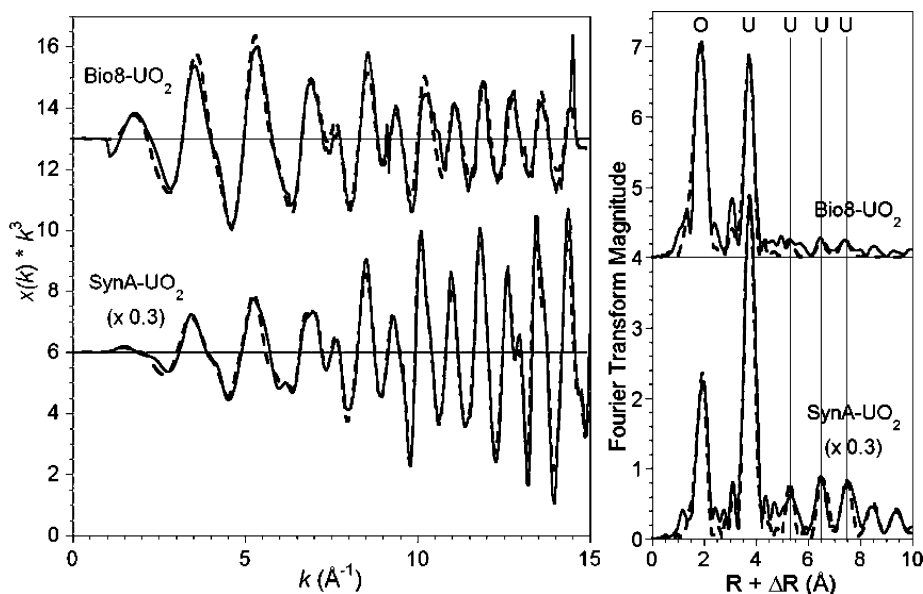
FIGURE 1. (a) Uranium L_3 edge EXAFS spectra (k^3 weighted) and (b) Fourier transform magnitude of bio8-UO_2 and synA-$UO_{2.00}$. Solid lines show experimental data, dashed lines represent the fit of structural data. Neighbor O- and U-shells appear at similar radial distance up to 8 Å ($R + \Delta R$) in both materials, and are visible beyond 8 Å in $UO_{2.00}$.
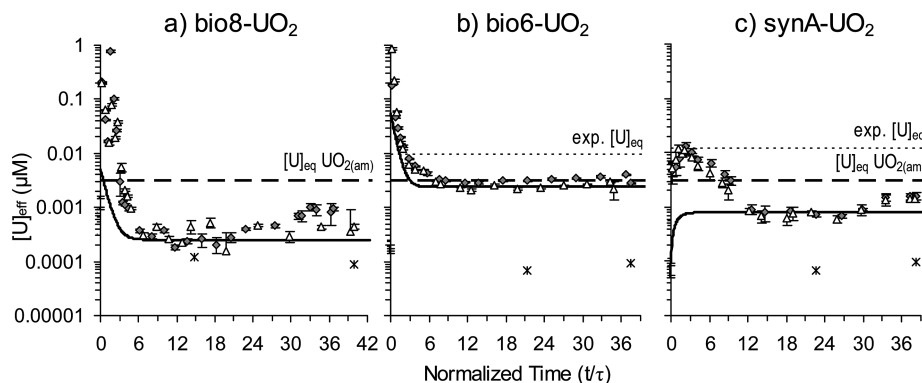

FIGURE 2. Dissolution of (a) bio8-UO_2, (b) bio6-UO_2, and (c) synA-UO_2 under reducing, carbonate-free conditions (pH 7.5 $\pm$ 0.2). Triangles and diamonds represent effluent concentrations of dissolved U of two replicate reactors as a function of normalized time ($\tau \sim$6 min). Error bars reflecting analytical standard deviation are mostly smaller than the symbol size. Stars show the U background concentration in the influent. The dotted and dashed lines indicate the equilibrium concentration, $[U]_{eq}$, determined experimentally and calculated from thermodynamics of a so-called amorphous UO_2 phase, respectively (cf. SI, Figure S5). The solid line illustrates the predicted response to the initial U load assuming a dissolution rate constant of (a) 1.0×10^{-14}, (b) 5.5×10^{-13}, and (c) 3.3×10^{-13} mol U m^{-2} s^{-1}.

a lower estimate because it does not account for surface roughness. *In-situ* SR-PD indicated lattice constants of 5.467 and 5.460 Å for lysozyme-treated bio8-UO_2 and bio6-UO_2, respectively, consistent with stoichiometric $UO_{2.00}$. After the treatment with NaOH solution, the unit cell constant diminished to 5.444 and 5.430 Å, indicating compression of the particles, presumably due to hydroxylation of the surface. SR-PD peak-fitting suggests a crystallite size of ~3.5 nm. The EXAFS oscillations and Fourier transforms of untreated bio8-UO_2 and synA-UO_2 show that U–U single scattering shells are present up to a distance of 8 and 10 Å ($R + \Delta R$), respectively. Albeit the intermediate-range order of the NaOH-treated bio-UO_2 materials appears weaker, the structures are consistent with that of stoichiometric $UO_{2.00}$ (Figure 1). Furthermore, the U–O shell distances of bio8-UO_2 (2.347 Å), bio6-UO_2 (2.336 Å), and syn-$UO_{2.00}$ (2.347 Å) are not distinguishable within the experimental error (*14*). There is no evidence for splitting of the U–O shell, as would be expected for UO_{2+x} ($x > 0$). These observations support a general structural homology between the bio-UO_2 samples and stoichiometric $UO_{2.00}$. The lack of U–U shells beyond 8 Å is attributed to a loss of long-range order in the nano-

particles beyond this distance. Details of the synchrotron-based structural characterization of bio-UO_2 are presented elsewhere (*14*).

Dissolution at Neutral pH Conditions. Dissolution rates of two biogenic and two synthetic UO_2 materials (Table 1) were determined from duplicate continuous flow experiments carried out in the absence of dissolved inorganic carbon (DIC) under reducing conditions at near neutral pH (7.2–8.0). The replicate results were in excellent agreement (Figure 2). Bio8-UO_2 and synA-UO_2 reached $[U]_{ss}$ of the same order of magnitude (0.2–0.8 nM). The $[U]_{ss}$ of bio6-UO_2 and synB-UO_2 (not shown) were about 1 order of magnitude higher. The mass-based dissolution rates of bio-UO_2 and syn-UO_2 ranged from 5×10^{-13} to 2×10^{-11} mol U g^{-1} s^{-1} (Table 2), spanning more than 2 orders of magnitude. When normalized to surface area, lower rates were found for the bio-UO_2 solids (1.1×10^{-14} to 3.4×10^{-13} mol U m^{-2} s^{-1}) than for the syn-UO_2 solids (2.8×10^{-13} to 2.1×10^{-12} mol U m^{-2} s^{-1}). The data of R_n (eq 3) are consistent with published dissolution rates of synthetic UO_2 materials (7.5×10^{-13} to 4.2×10^{-12} mol U m^{-2} s^{-1}, Table 2). Because the measured equilibrium solubility of bio6-UO_2 (9.5 nM) and synA-UO_2

TABLE 2. Comparison of UO₂ Dissolution Rates Measured under Reducing, Carbonate-Free Conditions (R_m and R_n are means Calculated by eqs 2 and 3; the Rate Constant k is Obtained from the Dissolution Model (eq 5) Assuming Steady-State Was Reached; All Rates Account for the Time-Dependent Loss of Solid while Dissolution)

UO₂ material	SSA (m²/g)	[solid] (g/L)	pH	influent electrolyte	R_m mol g⁻¹ s⁻¹	R_n mol m⁻² s⁻¹	k mol m⁻² s⁻¹	ref[b]
				experimental				
bio6-UO₂	50.14	1.15	7.60	1 mM HEPES	$4.94 \cdot 10^{-12}$	$9.85 \cdot 10^{-14}$	$2.50 \cdot 10^{-13}$	
bio6-UO₂	50.14	0.47	7.25	1 mM HEPES	$1.71 \cdot 10^{-11}$	$3.42 \cdot 10^{-13}$	$4.75 \cdot 10^{-13}$	
bio8-UO₂	50.14	1.60	7.67	1 mM HEPES	$5.35 \cdot 10^{-13}$	$1.07 \cdot 10^{-14}$	$1.17 \cdot 10^{-14}$	
bio8-UO₂	50.14	1.65	4.15	1 mM NaCl	$1.37 \cdot 10^{-08}$	$2.69 \cdot 10^{-10}$	N/A	
bio8-UO₂	50.14	1.56	3.10	1 mM HCl	$2.75 \cdot 10^{-08}$	$5.25 \cdot 10^{-10}$	N/A	
bio8-UO₂	50.14	1.40	2.15	10 mM HCl	$2.12 \cdot 10^{-08}$	$3.92 \cdot 10^{-10}$	$4.00 \cdot 10^{-10}$	
synB-UO₂	3.10	0.82	8.00	1 mM NaNO₃, TAPS	$1.25 \cdot 10^{-11}$	$4.03 \cdot 10^{-12}$	$1.33 \cdot 10^{-11}$	
synA-UO₂	5.93	0.79	7.70	1 mM HEPES	$3.27 \cdot 10^{-12}$	$5.51 \cdot 10^{-13}$	$8.75 \cdot 10^{-13}$	
synA-UO₂	5.93	1.25	7.25	1 mM HEPES	$1.66 \cdot 10^{-12}$	$2.80 \cdot 10^{-13}$	$3.17 \cdot 10^{-13}$	
synA-UO₂	5.93	1.35	5.20	1 mM NaCl	$3.27 \cdot 10^{-10}$	$5.52 \cdot 10^{-11}$	N/A	
synA-UO₂	5.93	1.35	4.10	1 mM NaCl	$8.32 \cdot 10^{-10}$	$1.40 \cdot 10^{-10}$	N/A	
synA-UO₂	5.93	1.33	3.10	1 mM HCl	$4.05 \cdot 10^{-09}$	$6.78 \cdot 10^{-10}$	$1.67 \cdot 10^{-09}$	
synA-UO₂	5.93	1.13	2.10	10 mM HCl	$3.85 \cdot 10^{-09}$	$6.38 \cdot 10^{-10}$	$6.67 \cdot 10^{-10}$	
				published dissolution rates obtained from CFR experiments on abiotic UO₂				
syn-UO₂.₀₀₁	0.201	0.5 g [a]	6.65	8 mM NaClO₄			$4.18 \cdot 10^{-12}$	(29)
syn-UO₂.₀₀₁	0.201	0.5 g [a]	7–11	8 mM NaClO₄			$1.90 \cdot 10^{-12}$	(29)
syn-UO₂	3.94	1.0	7.5	10 mM NaClO₄			$7.50 \cdot 10^{-13}$	(34)
SNF grains	0.03	230	5.8	10 mM NaCl			$1.46 \cdot 10^{-13}$	(15)

[a] A thin film of 0.5 g UO₂.₀ was used in this work. [b] If no reference given, data are from the present work.
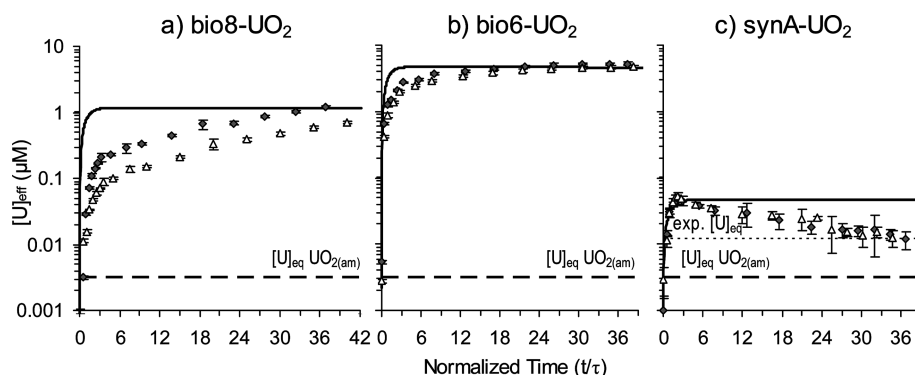

FIGURE 3. Dissolution of (a) bio8-UO₂, (b) bio6-UO₂, and (c) synA-UO₂ under reducing conditions in presence of 1 mM DIC (pH 8.1 ± 0.3). Triangles and diamonds represent effluent concentrations of dissolved U of two replicate reactors as a function of normalized time ($\tau \sim 6$–9 min). Error bars reflecting analytical standard deviation are mostly smaller than the symbol size. UO₂ dissolution was continued from the experiment shown in Figure 2. The dotted and dashed lines indicate the equilibrium concentration determined experimentally and calculated from thermodynamic data, respectively (cf. SI, Figure S5). In a U(VI) containing system, $[U]_{eq}$ of schoepite is predicted at 20–40 μM depending on pH and [DIC]. The solid line illustrates the predicted response to UO₂ dissolution with a rate constant of (a) 4.0×10^{-11}, (b) 1.75×10^{-10}, and (c) 2.7×10^{-11} mol U m⁻² s⁻¹.

(12 nM) was relatively close to $[U]_{ss}$ (Figure 2b and c), the reaction affinity must be considered when calculating intrinsic rate constants (k) for UO₂ dissolution. These values range from 1.2×10^{-14} to 4.8×10^{-13} mol U m⁻² s⁻¹ for the two bio-UO₂ materials, and from 3.2×10^{-13} to 1.3×10^{-11} mol U m⁻² s⁻¹ for the two syn-UO₂ materials.

The $[U]_{eq}$ obtained for bio6-UO₂ and synA-UO₂ was very similar, although the particle sizes of these two materials were quite different (Table 1). This similarity in equilibrium solubility is in accordance with the structural homology between bio-UO₂ and UO₂.₀₀ as determined by EXAFS and SR-PD (14), and suggests a minor impact of surface free energy on the solubility of nanoparticulate bio-UO₂ in water. The measured $[U]_{eq}$ values are slightly higher than those calculated from the NEA thermodynamic database considering UO₂(am) (19). The solubility of UO₂(am) was chosen as a reference and depicted in Figures 2 to 4 because this data is consistent with the best experimental solubility measurements carried out in aqueous solution at extremely low O₂ fugacity <10⁻⁶⁵ atm (20). The present paper will not address the intrinsic solubility of UO₂(cr) in water, which is still a matter of debate (21, 22).

All experiments showed an initial $[U]_{eff}$ peak immediately after the onset of UO₂ dissolution, which was higher for the bio-UO₂ materials ($\sim$1 μM) than for the syn-UO₂ materials ($\sim$0.02 μM). Such a transient pulse release of U is a common phenomenon of flow-through experiments and has been attributed to labile U(VI) on the UO₂ surface (23–25). The higher $[U]_{eff}$ peak for bio-UO₂ than syn-UO₂ is consistent with a greater surface area allowing more accumulation of U(VI) on the surface. Another possible explanation for the $[U]_{eff}$ peak is passage of colloidal UO₂ through the filter membrane during the first flush.

Carbonate Promoted Dissolution. The presence of carbonate is not expected to significantly alter the solubility of UO₂(am) in an anoxic system. For example, upon the addition of 1 mM inorganic carbon, the dissolved [U] would only increase from 3.16 to 3.24 nM (between pH 7.3 and 7.6) from the formation of aqueous U(IV)-carbonate complexes (19) (Figures S5 and S6, SI). However, if U(VI) is present, highly soluble U(VI) carbonate complexes will form (Figure S6b). Thus, if carbonate addition under reducing conditions
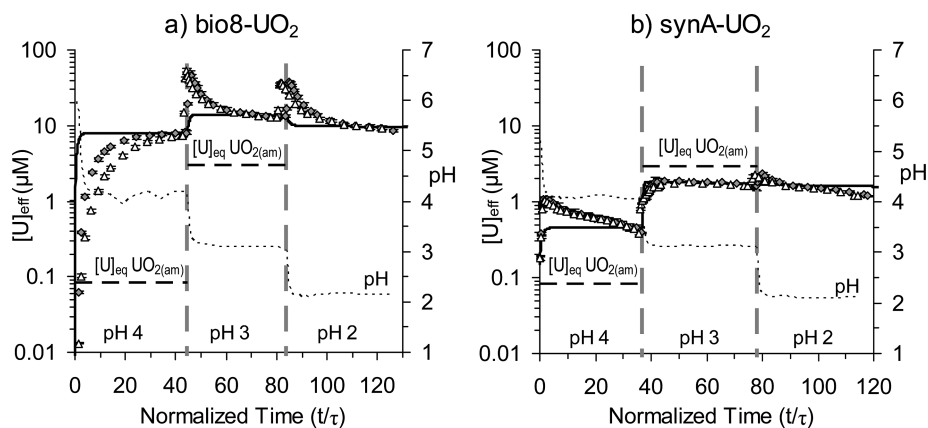
FIGURE 4. Dissolution of (a) bio8-UO$_2$ and (b) synA-UO$_2$ under reducing conditions at three consecutive pH levels. Triangles and diamonds represent effluent concentrations of dissolved U of two replicate reactors as a function of normalized time ($\tau \sim 6$ min). Error bars reflecting analytical standard deviation are mostly smaller than the symbol size. The dotted line represents the effluent pH based on the right ordinate. UO$_2$ dissolution was continued from anoxic dissolution at near neutral pH (bio8-UO$_2$) or pH 5 (synA-UO$_2$). The vertical dashed lines indicate the switch of influent pH, the horizontal dashed lines show the equilibrium concentration calculated for UO$_{2(am)}$ (cf. SI). At pH 2.2, $[U]_{eq}$ of UO$_{2(am)}$ is 263 μM, exceeding the limit of the left y-axis. The solid line illustrates the predicted response to UO$_2$ dissolution at rate constants of 2.8×10^{-10}, 5.3×10^{-10}, and 4.0×10^{-10} mol U m^{-2} s^{-1} for bio8-UO$_2$, and 1.5×10^{-10}, 1.7×10^{-9}, and 6.7×10^{-10} mol U m^{-2} s^{-1} for synA-UO$_2$, at pH 4, pH 3, and pH 2, respectively.

leads to a higher UO$_2$ dissolution rate, U(VI) must have continuously formed on the UO$_2$ surface by oxidation.

All tested UO$_2$ materials showed clear evidence of carbonate-induced U release (Figure 3). The increase in $[U]_{eff}$ upon the addition of carbonate spanned 2–3 orders of magnitude and was higher for the bio-UO$_2$ than for the synA-UO$_2$ material. For the latter, the step function increase in dissolution rate to 2.7×10^{-11} mol U m^{-2} s^{-1} was followed by a slowly declining net rate, with the $[U]_{eff}$ approaching the same $[U]_{eq}$ as determined earlier in carbonate-free solution (Figure 3c). This suggests that the detachment of U(VI) from the surface was faster than U(IV) oxidation, limiting the replenishment of U(VI) ions on the UO$_2$ surface. A similar dissolution pattern was observed for spent fuel in H$_{2(g)}$ saturated solution containing 10 mM NaHCO$_3$ (*15*). These results suggest that surface U(IV) oxidation occurred in the absence of carbonate, i.e., during the previous condition, and that UO$_2$ dissolution is controlled by a surface layer of U(VI) that accumulates over time and protects underlying U(IV) atoms from oxidation. According to the standard redox potential of U(VI)/U(IV) and H$^+$/H$_{2(aq)}$, U(IV) oxidation is thermodynamically favorable in pH 7 water up to a concentration of $\sim$7 nM dissolved U(VI) (*19*). Low but significant concentrations of dissolved H$_2$O$_2$ and O$_2$ on the order of 10^{-9} M can result from α-radiolysis of water at steady state and the given concentration of depleted U (*15, 26–28*). Natural U will lead to higher concentrations of oxidants due to higher concentrations of short-lived daughter products and their α/β-radiation.

In contrast to syn-UO$_2$, the $[U]_{eff}$ of the bio-UO$_2$ materials approached or reached steady state at much higher concentrations of >1 to 5 μM, more than 100 times higher than that measured for synA-UO$_2$. For the bio-UO$_2$, U(IV) oxidation cannot be rate-limiting. Rather the detachment of U(VI) or the dissolution of a U(VI) coating phase similar to schoepite (UO$_3 \cdot 2$H$_2$O) controls the net dissolution of bio-UO$_2$.

Proton Promoted Dissolution. The $[U]_{eff}$ increased considerably when the influent pH was lowered from near neutral to pH 4, pH 3, and pH 2 under reducing conditions (Figure 4). At pH 4, $[U]_{eff}$ of both UO$_2$ materials exceeded the calculated equilibrium solubility of UO$_{2(am)}$, with a greater difference for the bio8-UO$_2$ material. After switching to pH 3, $[U]_{eff}$ of bio8-UO$_2$ peaked at $\sim$50 μM and declined steadily thereafter, still exceeding the calculated equilibrium solubility of UO$_{2(am)}$. In contrast, $[U]_{eff}$ of synA-UO$_2$ responded in the predicted way to the step-function increase in UO$_2$ dissolution

rate, approaching $[U]_{ss}$ of $\sim$1.8 μM, which is below the calculated equilibrium solubility of UO$_{2(am)}$. At pH 2, the $[U]_{eff}$ pattern of bio8-UO$_2$ resembled the pattern seen at pH 3. For both UO$_2$ materials at pH 2, the $[U]_{eff}$ peak was followed by a slow decrease in $[U]_{eff}$ far below the calculated equilibrium solubility of UO$_{2(am)}$ of 263 μM.

An increase in UO$_2$ solubility is expected at acidic pH due to proton promoted hydrolysis (*19*). The hydrolysis reaction depends on the valence of surface bound U. Since U(VI) is likely to be formed on the UO$_2$ surface even under reducing conditions, hydrolysis of U(VI) rather than U(IV) is likely in cases where the equilibrium solubility of UO$_{2(am)}$ was exceeded. This reaction was most obvious for the bio-UO$_2$ material, which also dissolved faster in the presence of carbonate. The idea that hydrolysis reactions enhanced the detachment of U(VI) from the UO$_2$ surface is supported by nearly identical U(VI) and total U concentrations analyzed in the effluent of bio8-UO$_2$ even at a pH as low as 3. Although specific reasons for the transient $[U]_{eff}$ peaks are unknown, we hypothesize that rapid pH changes cause structural changes on the surface including bond breaks, and lead to instantaneous net loss of U.

Figure 5 shows the dissolution rates of synA-UO$_2$ and bio8-UO$_2$ plotted as a function of pH. The rates were highly consistent below pH 6 when normalized to surface area (Figure 5b). This implies a similar number and reactivity of sites per unit surface area. For the pH range between 3 and 8, the dissolution of synA-UO$_2$ can be described by a log-linear relationship (eq 6) with the standard error presented as the uncertainty.

$$R_n(\text{mol m}^{-2}\text{s}^{-1}) = 8.3 \pm 3.2 \times 10^{-8}[\text{H}^+]^{0.66 \pm 0.03} \quad (3 \le \text{pH} \le 8)$$
$$(6)$$

A similar relationship was reported for proton promoted dissolution of synthetic UO$_2$ at reducing conditions, with R_n (mol m^{-2} s^{-1}) = $1.4(\pm 0.3) \times 10^{-8}$ [H$^+$]$^{0.53 \pm 0.08}$ (*29*). The fractional reaction order between 0 and 1 is consistent with dissolution of other metal oxide surfaces under acidic conditions. The reaction order was found to be fractional if the dissolution rate depends on the activity of H$^+$ adsorbed to the surface (*30*). To compare the dissolution kinetics of common soil minerals and syn-UO$_2$, the latter was found to dissolve at least 1 order of magnitude faster at pH 3 to 6 than biotite [KMgFe$_2$AlSi$_3$O$_{10}$(OH)$_2$] or goethite (α-FeOOH) (*31*).
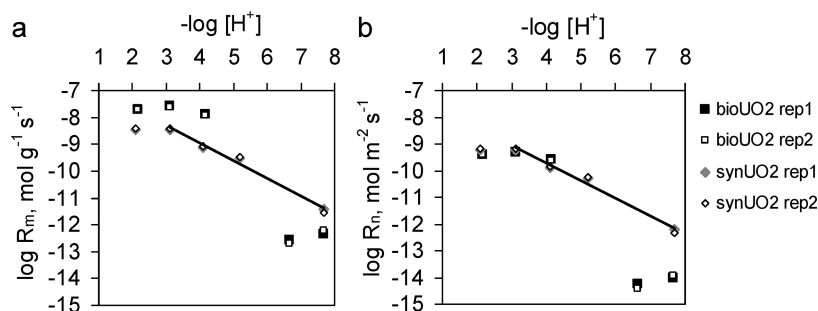
FIGURE 5. Dissolution rates of two replicates of bio8-UO_2 and synA-UO_2 solids as a function of pH under reducing conditions in the absence of carbonate. (a) Rates R_m given per unit mass and time, and (b) R_n normalized to surface area. The lines show the linear regression of synA-UO_2 dissolution rates from pH 3 to 8, which yielded a correlation coefficient (r^2) of 0.985.

Implications for Remediation. Different processes contribute to the dissolution of biogenic UO_2 in reducing environments: (i) proton attack on the UO_2 surface dissolving U(IV) aqueous species, the rate of which is a function of pH and site density, (ii) continuous oxidation of surface-exposed U(IV) to U(VI), where the rate depends on the activity of trace oxidants and accessible U(IV) sites, and (iii) detachment of surface bound U(VI) into solution, which is a function of pH and activity of complexing agents such as carbonate. The experimental data suggest that in reducing environments UO_2 dissolution is primarily controlled by the detachment of U(VI) ions. The formation of a thin surface layer of U(VI) by either adsorption or surface oxidation is generally fast and thermodynamically favorable in water. Surface oxidation can also result from trace amounts of oxidants formed by α-radiolysis of water. The presence of an outer layer of U(VI) on the UO_2 surface is consistent with structural investigations of this material that suggest the presence of short-range structural disorder in the outer zone of bio-UO_2 in a fashion reminiscent of that in UO_{2+x}, which surrounds a core of well-ordered stoichiometric $UO_{2.00}$ (*14*).

Hence, if surface U(VI) is controlling UO_2 dissolution, then carbonate will play a major role in U immobilization and subsurface transport. By simulating a moderate DIC concentration representative of groundwater, dissolution rates of bio-UO_2 and dissolved U concentrations increased by 3 orders of magnitude compared to carbonate-free anoxic water. When applying the measured dissolution rates to field conditions, interactions of bio-UO_2 with other groundwater constituents including organic matter, Ca, Mg, Fe, and Mn must also be considered. For instance, organic matter, including biomass produced by the bacteria, may coat the bio-UO_2 particles and consume oxidants, thus retarding the oxidative dissolution of UO_2. The formation of ternary U(VI)−CO_3−Ca/Mg complexes in the system (*32*) can increase the stability of U(VI), and cations may adsorb on the bio-UO_2 particles and modify their solubility and dissolution kinetics. Analogous to Fe(III) (hydr)oxides (*10*), microbially generated Mn(III/IV) oxides may in turn oxidize UO_2 and thus decrease the stability of bio-UO_2 (*33*). Despite this increased environmental complexity, the intrinsic properties of bio-UO_2 provide a strong basis for estimating the stability of such nanoparticulate materials. Taking into account the residence time of undisturbed groundwater on the order of decades or centuries (*29*), it can be expected that UO_2 dissolution in such waters will be controlled by thermodynamics rather than kinetics, in particular by the thermodynamics of U(VI) species. Thus, in order to control U mobility in the subsurface, strategies are required to maintain strictly reducing conditions, sustain active anaerobic microbial populations, or increase the structural stability of biogenic UO_2.

Supporting Information Available
Detailed description of material preparation, experimental setup, modeling approach, structural characterization, and thermodynamic calculations (including 6 figures and 2 tables). This material is available free of charge via the Internet at http://pubs.acs.org.

Literature Cited
(1) Janeczek, J.; Ewing, R. C. Dissolution and alteration of uraninite under reducing conditions. *J. Nucl. Mater.* **1992**, *190*, 157–173.

(2) Finch, R. J.; Ewing, R. C. The corrosion of uraninite under oxidizing conditions. *J. Nucl. Mater.* **1992**, *190*, 133–156.

(3) Lovley, D. R.; Phillips, E. J. P.; Gorby, Y. A.; Landa, E. R. Microbial reduction of uranium. *Nature* **1991**, *350*, 413–416.

(4) Lovley, D.; Phillips, E. J. P. Reduction of uranium by *Desulfovibrio desulfuricans*. *Appl. Environ. Microbiol.* **1992**, *58*, 850–856.

(5) Tebo, B. M.; Obraztsova, A. Y. Sulfate-reducing bacterium grows with Cr(VI), U(VI), Mn(IV), and Fe(III) as electron acceptors. *FEMS Microbiol. Lett.* **1998**, *162*, 193–198.

(6) Lovley, D. R.; Phillips, E. J. P. Bioremediation of uranium contamination with enzymatic uranium reduction. *Environ. Sci. Technol.* **1992**, *26*, 2228–2234.

(7) Anderson, R. T.; Vrionis, H. A.; Ortiz-Bernad, I.; Resch, C. T.; Long, P. E.; Dayvault, R.; Karp, K.; Marutzky, S.; Metzler, D. R.; Peacock, A.; White, D. C.; Lowe, M.; Lovley, D. R. Stimulating the in situ activity of Geobacter species to remove uranium from the groundwater of a uranium-contaminated aquifer. *Appl. Environ. Microbiol.* **2003**, *69*, 5884–5891.

(8) Senko, J. M.; Istok, J. D.; Suflita, J. M.; Krumholz, L. R. In-situ evidence for uranium immobilization and remobilization. *Environ. Sci. Technol.* **2002**, *36*, 1491–1496.

(9) U.S. EPA. National Primary Drinking Water Regulations; Radionuclides; Final Rule. 2000, 40 CFR Parts 9, 141, and 142. Fed. Regist. Vol. 65: 76707–76753.

(10) Ginder-Vogel, M.; Criddle, C. S.; Fendorf, S. Thermodynamic constraints on the oxidation of biogenic U(IV) (hydr)oxides. *Environ. Sci. Technol.* **2006**, *40*, 3544–3550.

(11) Senko, J. M.; Kelly, S. D.; Dohnalkova, A. C.; McDonough, J. T.; Kemner, K. M.; Burgos, W. D. The effect of U(VI) bioreduction

kinetics on subsequent reoxidation of biogenic U(IV). *Geochim. Cosmochim. Acta* **2007**, *71*, 4644–4654.

(12) Wan, J. M.; Tokunaga, T. K.; Brodie, E.; Wang, Z. M.; Zheng, Z. P.; Herman, D.; Hazen, T. C.; Firestone, M. K.; Sutton, S. R. Reoxidation of bioreduced uranium under reducing conditions. *Environ. Sci. Technol.* **2005**, *39*, 6162–6169.

(13) Suzuki, Y.; Kelly, S. D.; Kemner, K. M.; Banfield, J. F. Nanometre-size products of uranium bioreduction. *Nature* **2002**, *419*, 134–135.

(14) Schofield, E.; Veeramani, H.; Sharp, J.; Suvorova, E.; Bernier-Latmani, R.; Mehta, A.; Stahlman, J.; Clark, D. L.; Conradson, S. D.; Webb, S.; Bargar, J. R. Structure of biogenic uraninite produced by Shewanella oneidensis, strain MR-1. *Environ. Sci. Technol.* **2008**. (accepted).

(15) Röllin, S.; Spahiu, K.; Eklund, U. B. Determination of dissolution rates of spent fuel in carbonate solutions under different redox conditions with a flow-through experiment. *J. Nucl. Mater.* **2001**, *297*, 231–243.

(16) Johnson, D. A.; Florence, T. M. Spectrophotometric determination of uranium(VI) with 2-(5-bromo-2-pyridylazo)-5-diethylaminophenol. *Anal. Chim. Acta* **1971**, *53*, 73–79.

(17) Webb, S. M. SIXPack: a Graphical User Interface for XAS Analysis Using IFEFFIT. *Phys. Scr.* **2005**, *T115*, 1011–1014.

(18) Ankudinov, A. L.; Ravel, B.; Rehr, J. J.; Conradson, S. D. Real-space multiple-scattering calculation and interpretation of x-ray-absorption near-edge structure. *Phys. Rev. B Condensed Matter* **1998**, *58*, 7565–7576.

(19) Guillaumont, R.; Fanghänel, T.; Fuger, J.; Grenthe, I.; Neck, V.; Palmer, D. A.; Rand, M. H. *Update on the Chemical Thermo-dynamics of Uranium, Neptunium, Plutonium, Americium and Technetium*; OECD Nuclear Energy Agency; Elsevier: Amsterdam, 2003.

(20) Rai, D.; Felmy, A. R.; Ryan, J. L. Uranium(IV) hydrolysis constants and solubility product of $UO_2 \cdot xH_2O(am)$. *Inorg. Chem.* **1990**, *29*, 260–264.

(21) Neck, V.; Kim, J. I. Solubility and hydrolysis of tetravalent actinides. *Radiochim. Acta* **2001**, *89*, 1–16.

(22) Fanghänel, T.; Neck, V. Aquatic chemistry and solubility phenomena of actinide oxides/hydroxides. *Pure Appl. Chem.* **2002**, *74*, 1895–1907.

(23) dePablo, J.; Casas, I.; Gimenez, J.; Marti, V.; Torrero, M. E. Solid surface evolution model to predict uranium release from unirradiated UO_2 and nuclear spent fuel dissolution under oxidizing conditions. *J. Nucl. Mater.* **1996**, *232*, 138–145.

(24) Gimenez, J.; de Pablo, J.; Torrero, M. E.; Casas, I. Conceptual and mathematical model for the $UO_{2(s)}$ dissolution in brines under different redox conditions. *Radiochim. Acta* **1997**, *78*, 21–25.

(25) Pierce, E. M.; Icenhower, J. P.; Serne, R. J.; Catalano, J. G. Experimental determination of $UO_{2(cr)}$ dissolution kinetics: Effects of solution saturation state and pH. *J. Nucl. Mater.* **2005**, *345*, 206–218.

(26) Christensen, H.; Sunder, S.; Shoesmith, D. W. Oxidation of nuclear fuel (UO_2) by the products of water radiolysis: development of a kinetic model. *J. Alloys Compd.* **1994**, *213/214*, 93–99.

(27) Suzuki, T.; Abdelouas, A.; Grambow, B.; Mennecart, T.; Blondiaux, G. Oxidation and dissolution rates of $UO_{2(s)}$ in carbonate-rich solutions under external alpha irradiation and initially reducing conditions. *Radiochim. Acta* **2006**, *94*, 567–573.

(28) Kubatko, K. A. H.; Helean, K. B.; Navrotsky, A.; Burns, P. C. Stability of peroxide-containing uranyl minerals. *Science* **2003**, *302*, 1191–1193.

(29) Bruno, J.; Casas, I.; Puigdomenech, I. The Kinetics of Dissolution of UO_2 under Reducing Conditions and the Influence of an Oxidized Surface-Layer (UO_{2+x}) - Application of a Continuous Flow-through Reactor. *Geochim. Cosmochim. Acta* **1991**, *55*, 647–658.

(30) Lasaga, A. C. Fundamental approaches in describing mineral dissolution and precipitation rates. In *Chemical Weathering Rates of Silicate Minerals*; White, A. F., Brantley, S. L., Eds.; Mineralogical Society of America: Washington, DC, 1995; Vol *31*, pp 23−86.

(31) Stumm, W.; Morgan, J. J. *Aquatic Chemistry*, 3rd ed.; John Wiley & Sons, Inc.: New York, 1996.

(32) Dong, W. M.; Brooks, S. C. Determination of the formation constants of ternary complexes of uranyl and carbonate with alkaline earth metals (Mg^{2+}, Ca^{2+}, Sr^{2+}, and Ba^{2+}) using anion exchange method. *Environ. Sci. Technol.* **2006**, *40*, 4689–4695.

(33) Chinni, S.; Anderson, C.; Ulrich, K.-U.; Giammar, D. E.; Tebo, B. M. Indirect UO_2 oxidation by Mn(II)-oxidizing spores of Bacillus sp. strain SG-1 and the effect of U and Mn concentrations. *Environ. Sci. Technol.* 2008. (submitted).

(34) Frazier, S. W.; Kretzschmar, R.; Kraemer, S. M. Bacterial siderophores promote dissolution of UO_2 under reducing conditions. *Environ. Sci. Technol.* **2005**, *39*, 5709–5715.

ES800647U